JASA ARTICLE

Observations and simulations of caustic formation due to oceanographic fine structure

Jacob P. DeFilippis,[a] Bruce D. Cornuelle, Andrew J. Lucas,[b] William S. Hodgkiss, Luc Lenain, W. A. Kuperman, and Matthew H. Alford

Scripps Institution of Oceanography, University of California at San Diego, La Jolla, California 92093, USA

ABSTRACT:
An at-sea experiment in deep water was conducted to explore the impact of small-scale sound-speed variability on mid-frequency (1–10 kHz) acoustic propagation. Short-range (1–5 km) acoustic transmissions were sent through the upper ocean (0–200 m) while oceanographic instruments simultaneously measured the ocean environment within 2 km of the single upper turning points of the acoustic transmissions. During these transmissions, acoustic receptions over a 7.875 m vertical line array show closely spaced, sometimes interfering arrivals. Ray and full-wave simulations of the transmissions using nearby sound-speed profiles are compared deterministically to the received acoustic signals. The sensitivity of the acoustic arrivals to the vertical scales of ocean sound speed is tested by comparing the observed and simulated arrival intensity where the sound-speed profile used by the simulation is smoothed to varying scales. Observations and modeling both suggest that vertical fine-scale structures (1–10 m) embedded in the sound-speed profile have strong second derivatives which allow for the formation of acoustic caustics as well as potentially interfering acoustic propagation multipaths. *© 2023 Acoustical Society of America.*

https://doi.org/10.1121/10.0020830

(Received 27 December 2022; revised 18 July 2023; accepted 13 August 2023; published online 5 September 2023)

[Editor: D. Benjamin Reeder] Pages: 1372–1388

I. INTRODUCTION

Both deep and shallow water ocean acoustic experiments have shown that acoustic travel-time variability can be related deterministically to sound-speed perturbations from oceanographic processes such as internal tides and mesoscale eddies,[1–3] and that phase and amplitude fluctuations of ocean acoustic receptions can be related statistically to the spectrum of internal waves.[1,4,5] Although these oceanographic processes are responsible for most of the acoustic travel time, phase, and amplitude fluctuations, at time scales ranging from hours to days, small-scale (1–10 m) variations in the vertical sound-speed gradient, generally referred to as fine structure,[6,7] can alter the acoustic phase and amplitude fluctuations from those same processes.[8,9] Acoustic propagation effects such as caustic formation and micro-multipathing have been attributed to fine structure,[4,10] but a deterministic comparison between observed and modeled acoustic propagation through oceanographic fine structure has not been done. The observations and modeling in this paper show that sections of the sound-speed profile with strong second derivatives due to the small-scale structure in the ocean can triplicate ray paths. Consequently, those triplicated rays result in multiple acoustic arrivals with a small time of arrival separation at the receiver.

Previous mid-frequency ocean acoustic experiments,[5,11,12] transmitting at ranges less than 40 km with broadband pulses, looked at phase and amplitude fluctuations in relation to predicted sound-speed fluctuations from internal waves. Acoustic fluctuations are severe for mid-frequency (1–10 kHz) acoustic propagation through the upper ocean because the acoustic wavelength approaches the scale of the fine structure in the ocean.[4] The simulated acoustic phase and amplitude statistics were less like the observed phase and amplitude statistics when the fine structure was removed from the sound-speed profile.[9] This disagreement worsened as frequency increased. This comparison suggested that fine-structure measurements would be crucial to making a quantitative comparison between acoustic fluctuations and internal waves, particularly for mid-frequency acoustic propagation.

In these experiments, pulse arrivals that were identified with individual eigenrays computed from a time-averaged sound-speed profile would often appear to be comprised of multiple overlapping pulse arrivals. The time-averaging of the sound-speed profile tends to remove small-scale sound-speed structures because of their time-varying depths due to internal waves. Hence, fine vertical scales of the sound-speed profile were theorized to allow for multiple pulse arrivals that came from additional ray paths that were adjacent in launch angle to the unperturbed path calculated from the time-averaged profile.[4] These nearby ray paths are frequently called micro-multipaths or microrays[13] which originate from caustic formation/ray triplication discussed further in Sec. IV.

Parts of the recorded acoustic arrivals from the Slice89 experiment,[8] which transmitted 250 Hz center frequency

---

[a] Email: jdefilip@ucsd.edu

[b] Also at: Department of Mechanical and Aerospace Engineering, University of California at San Diego, La Jolla, CA, 92093, USA.

broadband pulses at 1000 km in range, were also associated with ray triplication from oceanographic fine structure.[10] The relative curvature of the sound-speed profile, $U(z) = c(z)\partial_{zz}c(z)/(\partial_z c(z))^2$, was suggested as a dimensionless parameter for inferring caustic formation by Duda and Bowlin.[10] This parameter is useful for evaluating when curvature in the profile is likely to form caustics and consequently triplications in the timefront. $U(z)$ can be singular and highly variable, so the moments of its distribution are often more relevant. Normally $U(z)$ is reported as the logarithm of its absolute value, $U_{10} = \log_{10}(|U(z)|)$.

In order to study the influence of ocean fine structure on mid-frequency acoustic propagation at sub-hourly time scales, we conducted a joint ocean acoustics/physical oceanography experiment offshore of Southern California. The experiment, described in Sec. II, used shipboard and semi-autonomous sampling to provide measurements of the environment near the sound transmission paths (less than 2 km). Pulses of sound at 1–10 kHz were transmitted along paths of 1–5 km in length. Both oceanographic and acoustic observations from the experiment are described in Sec. III.

Modeling the effects of vertical fine structure on the acoustic propagation, described in Sec. IV, with a deterministic approach is possible because of the proximity of the oceanographic measurements to the short-range acoustic propagation paths that have single turning points. A deterministic approach was previously used by other researchers to model travel time fluctuations caused by perturbations to the sound-speed field from a large non-linear internal wave[3] and model the attribution of caustics in shallow-water acoustic communication experiments with rays reflecting from ocean surface gravity waves,[14] which is a motivation for this study. Caustics and triplicated ray paths from surface waves were found to complicate signal processing to varying degrees based on the shape of the sea surface.[15] The comparison between observations and model, described in Sec. V, identifies features in the sound-speed profile that cause interfering arrivals in the acoustic observations.

II. METHODS

A. Experimental setup

The at-sea experiment took place from 5 to 25 May 2021 on the R/V Roger Revelle in deep water 450 km from the coast of Southern California. The experiment site is outlined by the box shown in Fig. 1. This site was chosen to sample a region without bathymetric features that would have affected the acoustic propagation or oceanography such as acoustic bottom reflection or local internal tide generation.

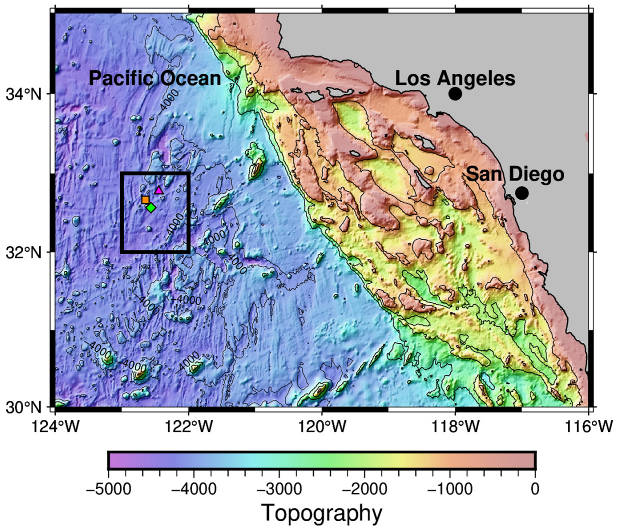

FIG. 1. (Color online) A bathymetric map showing the location of the experiment inside the box. The site is approximately 450 km from San Diego, off of the continental shelf with a bottom depth of roughly 4000 m. The locations of the three acoustic transmissions discussed in this paper are marked with a green diamond, purple triangle, and orange square.

Acoustic transmissions were made at roughly fixed ranges from 1 to 5 km from a single shipboard acoustic source to a single drifting vertical line array with 64 elements. The array had an aperture of 7.875 m with uniform 0.125 m hydrophone spacing. The nominal depth of the acoustic source was 200 m and the nominal receiver array center depth was 132 m, with most of the received sound traveling through the upper 200 m of the ocean. Figure 2 shows a schematic of the acoustic experiment setup with an example of the acoustic ray paths calculated with a ray trace model using sound-speed data from the experiment.

Both continuous wave and maximum length sequences (MLS) forming pseudo-pulses were transmitted at a 156 dB re $1\,\mu\mathrm{Pa}^2$ source level. These transmissions were in the acoustic mid-frequency band (1–10 kHz) so that the acoustic propagation would interact more with the fine-scale features of the ocean environment. Maximum length sequences were used to modulate the phase of the 4 kHz carrier frequency with a 4 kHz bandwidth. The repetition rate of the sequence is set by the MLS length of 63.5 ms with 2 cycles per digit. The hydrophones on the receiver array have high-pass poles at 100 Hz and 500 Hz attenuating low-frequency ambient noise. The receiver array data acquisition system samples the hydrophone time series at 25 kHz. A set of maximum length sequences was matched-filtered to calculate the travel time, phase, Doppler shift, and intensity of the arrivals. After conditioning the signal and applying the matched filter the SNR of the pulse is approximately 15 dB. The peak arrival time uncertainty of roughly 0.3 ms is calculated using the bandwidth and SNR of the pulses.[16] The time precision and vertical resolution of these measurements allow us to probe the fine scales of acoustic fluctuations. Further information on the MLS performance can be found in Ref. 17.

The background characteristics of the sound speed in the operating area were supplied by four drifting Wire Walkers and the shipboard FastCTD. Wire Walkers[18–20] are drifting oceanographic sampling platforms carrying a CTD that profiled between 0 and 500 m depth of temperature, salinity, and pressure roughly every 30 min with 0.25 m vertical resolution. Wire Walkers were deployed in an array encompassing the acoustic instruments. The distance between drifting Wire Walkers was initially set between

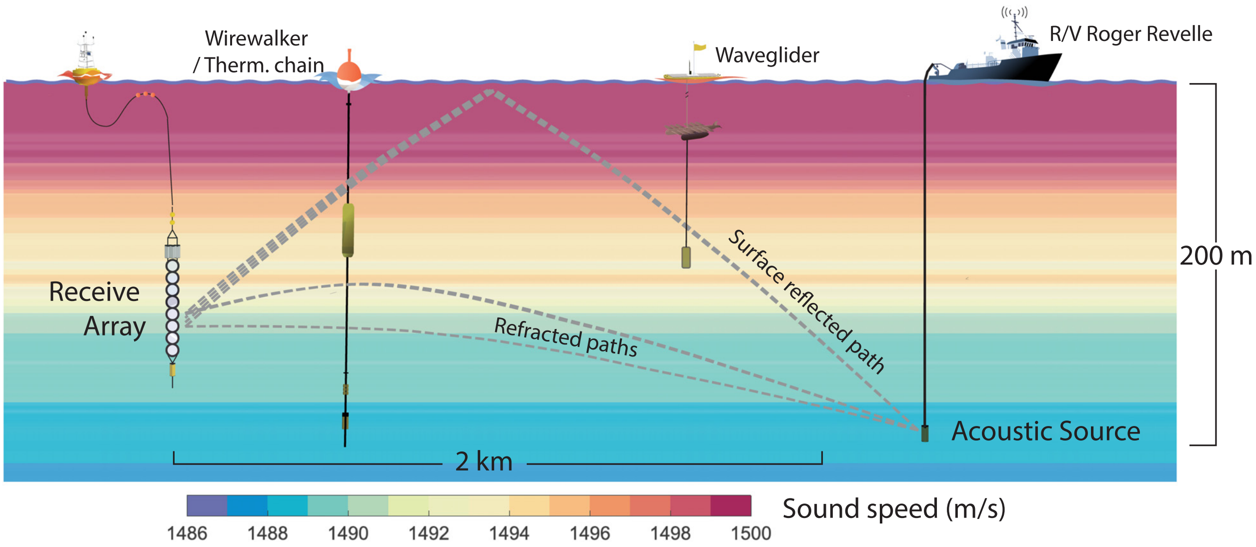

FIG. 2. (Color online) A typical instrumental setup for acoustic transmissions during the experiment. The acoustic source and array center were at depths of 200 m and 132 m respectively, separated by approximately 2 km in range. A drifting thermistor chain and Wave Glider platform measured sound speed nearby the turning point of acoustic ray paths. The gray dashed lines mark ray paths that intersect both source and receiver. The ray paths were calculated using a sound-speed profile shown with the background layers of color. The sound speed was measured by a drifting thermistor chain on 7 May 20:20.

5 and 10 km. The FastCTD, a rapid shipboard profiling platform, measured temperature, salinity, and pressure when the acoustic source was not transmitting. This platform can profile 0–300 m depth at a roughly 0.1 m vertical resolution every three minutes.[21] Measurements from these instruments were used to calculate vertical correlation length scales and the statistical relationship between temperature and salinity in the region, while two thermistor chains and a Wave Glider provided direct measurements of the sound-speed profile near the transmission path.

The two drifting thermistor chains, TC5 and TC7, were deployed 1–2 km away from the drifting receiver array. Both thermistor chains spanned 0–200 m in depth. TC5 had thermistors placed every 2 m in depth with pressure sensors every 25 m between 0 and 200 m. TC5 thermistors had a 0.1 ms thermal response time and a 2 Hz sampling rate. TC7 had a hybrid configuration with both thermistors and a Wire Walker deployed on the chain. TC7 had thermistors placed every 3 m in depth with pressure sensors every 25 m between 0 and 50 m and 100–200 m depth. TC7 thermistors had a 1 s thermal response time and a one-minute sampling rate. The TC7 Wire Walker profiled between 50 and 100 m depth along the chain. At these depths, the Wire-Walker CTD profiled salinity, temperature, and pressure with 0.25 m vertical resolution every 15–20 min.

The *in situ* temperature profiles, $T(P)$, from the thermistor chain, were converted into sound-speed estimates $c(P)$ by constructing an empirical relationship between salinity and temperature $S(T)$. Once $S(T)$ was calculated, the sound-speed estimate was calculated via the equation of state $c(P) = c_{eos}(S(T(P)), T(P), P)$.[22] The error due to the absence of *in situ* salinity measurements, discussed later in this section, is on average less than 0.1 m/s. The pressure coordinate, P was converted into depth from the mean sea surface rendering a sound-speed profile $c(z)$.

The Wave Glider, a piloted semi-autonomous vehicle,[23,24] profiled temperature, salinity, and pressure with a CTD every 10 min between 50 and 130 m depth with roughly 0.15 m vertical resolution. This depth range spans the turning depths of acoustic rays that were received by the array. The Wave Glider was positioned precisely between the acoustic source and receiver array for some of the acoustic transmissions. The drifting thermistor chains and the Wave Glider's profiling CTD were used to estimate the sound-speed field near the midpoint of the acoustic transmissions.

Three acoustic transmissions with simultaneous nearby sound-speed profiles were chosen to demonstrate the relationship between fine structure and interfering acoustic multi-paths. These acoustic transmission periods are highlighted because they were at relatively short ranges (less than 3 km) and the thermistor chains or Wave Glider were sampling close to the turning points of the ray paths. These transmissions took place on 7 May from 18:52 to 21:35, 10 May from 20:00 to 22:15, and 17 May from 18:00 to 19:45. All times are reported in UTC. Labels T1, T2, and T3 are given to minute-long blocks of continuous transmissions for 7 May 20:22, 17 May 19:10, and 10 May 20:30, respectively. These labels are ordered by transmission range. Figure 3 shows the GPS tracks of both the acoustic and oceanographic instruments during the transmission period with a line and the GPS position at T1, T2, and T3 with a circle marker.

III. DATA

A. Sound-speed observations

Sound-speed measurements from the Wave Glider, TC5, and TC7, shown in Figs. 4(a), 4(b), and 4(c), correspond to the minute-long transmission intervals T1, T2, and

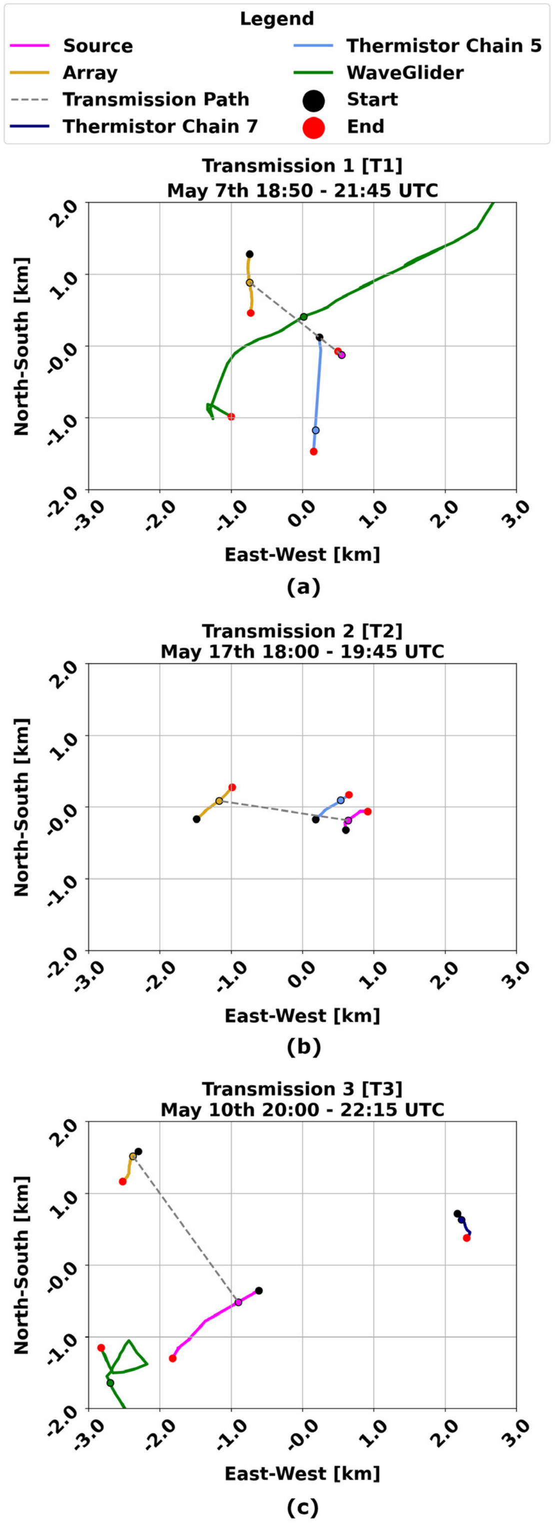

FIG. 3. (Color online) The GPS positions of the drifting receiver array (gold line), the acoustic source on the R/V Roger Revelle (magenta line), drifting thermistor chains (dark and light blue lines), and the Wave Glider (green line). Each line has a red and black dot that indicates the start and end position of each track. (a), (b), (c) GPS tracks on 7 May from 18:52 to 21:35, 17 May from 18:00 to 19:45, and from 10 May from 20:00 to 22:15, respectively. A circle marker with the same color as the track line is drawn for minutes 7 May 20:22, 17 May 19:10, and 10 May 20:30 for (a)–(c) to mark transmissions T1, T2, and T3 respectively. A transmission line is also drawn from source to receiver at those transmission times (gray dashed line).

T3 in Figs. 3(a), 3(b), and 3(c), respectively. Sound-speed profiles are made by interpolating through the sound-speed measurements from those instruments. In Secs. IV and V, these sound-speed profiles are input into acoustic propagation models to connect the observed acoustic arrivals to the observed oceanographic structure.

The thermistors were affected by the surface wave action on the thermistor chain surface buoy. The thermistors were displaced vertically at depth, although, the displacement was vertically coherent implying that the chain acted stiffly. This displacement was typically 1–2 m over 10 s. The combination of this displacement and the 2 Hz sampling rate for thermistors on TC5 was utilized to form a synthetic aperture by grouping minute-long intervals of thermistor data (light blue dots) to produce a temperature profile every minute. This minute-long interval of temperature samples filled in the vertical gaps between thermistors along the chain and provided a nearly continuous profile with an 0.02 m average vertical resolution. The synthetic aperture could not be used for thermistors on TC7 (dark blue dots) which had a one-minute sampling.

During transmissions T1 and T3, the Wave Glider measurements (green dots) were closer to the acoustic transmission path than measurements from TC5 and TC7, which were roughly 1–4 km away from the transmission path. Outside the Wave Glider's profiling range, 50–130 m, the thermistor chain measurements were used to fill in the sound-speed profile from 130 to 200 m and from the 0–50 m depth. We believe using two horizontally separated estimates of sound speed for the propagation modeling is justified because the sound speed at the depths filled in by the thermistor chain does not vary as strongly (see Fig. 4), and the acoustic propagation was not as sensitive to changes in the sound speed at those depths compared to depths of 50–130 m.

Sound-speed measurements from the thermistor chain and Wave Glider were least squares fit to a cubic spline to create a twice-differentiable sound-speed profile, shown in Fig. 4 as the black and white dashed line. The spline is comprised of piece-wise third-order polynomials.[25] The coefficients of each piece-wise polynomial are defined over a finite interval. The boundary of each interval is called a knot. At each knot, the value, first, and second derivative of the neighboring piece-wise polynomials must be equal which enforces the continuity of the spline. The cubic splines had an approximately 2 m knot spacing which enforced polynomial smoothness in the sound speed over 2 m scales. This scale was chosen so that the splines would not overfit the data but at the same time model the meter-scale vertical sound-speed structures.

We assume internal waves are the dominant process driving the temporal sound-speed variability at sub-hourly time scales represented by the hour-long standard deviation (blue bars) to the mean sound speed as measured by TC5 and TC7 in Figs. 4(a)–4(c). The sound-speed fluctuation, $\delta c(z)$, at a depth z from the mean sound speed results from vertically varying internal wave vertical displacement $\zeta(z)$

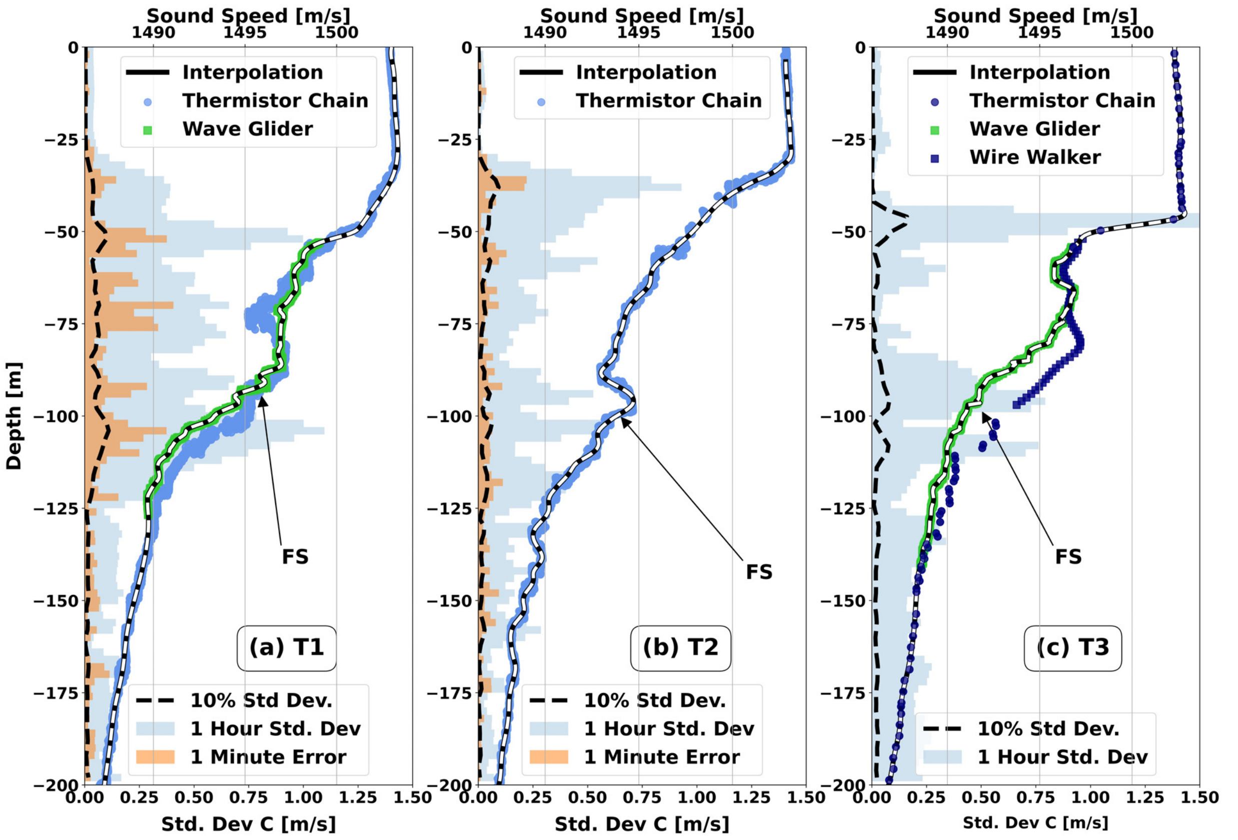

FIG. 4. (Color online) Sound-speed profiles during transmission T1, T2, and T3 are made from sound-speed estimates collected by thermistors on TC5 (light blue dots), thermistors on TC7 (dark blue dots), the profiling Wire Walker CTD on TC7 (dark blue squares), and the profiling Wave Glider CTD (green squares). A cubic spline (black and white dashed line) was fit to a minute-long collection of the sound-speed estimates. The labels "FS" point out a few examples of fine structure in the sound-speed profile. The top and bottom horizontal axis shows the scales for sound speed and sound-speed deviation. The standard deviation of sound speed (blue bars) over an hour and the root mean square misfit (orange bars) of the spline over a minute are binned into one-meter depths along the left vertical axis. The black dashed line on the left side of each figure is 10% of the hour-long standard deviation. (c) T3 does not have an interpolation error because this particular thermistor chain had a one-minute sampling rate.

of the potential sound-speed profile $c(z)$. This fluctuation is described in Eq. (1),

$$\delta c(z) = c(S(z), T_p(z), P(z)) - c(S(z-\zeta(z)), T_p(z-\zeta(z)), P(z)), \tag{1}$$

where S is salinity, P is pressure, and T_p is potential temperature.

The root mean square (RMS) residuals from the spline fit to a minute-long set of sound-speed observations measured by TC5 are shown in Figs. 4(a) and 4(b) (orange bars). The residuals are the difference between the fitted spline curve and the sound-speed point observations. The differences are mostly due to bias from fitting to a spline curve to the measurements which may have sharper curvature. The change in sound speed over a minute from the internal waves is expected to be small because of the drop in internal wave displacement power at the maximum buoyancy frequency N,[26] which was about 4 cycles per hour in the experiment region.

The sound-speed profiles in Fig. 4 have depths where strong and weak sound-speed derivatives alternate, appearing as steps along the sound-speed profile. The second derivative of sound speed is strongest at the edge of each fine-structure step, where the first derivative abruptly changes from strong to weak or vice versa over a small vertical distance. Parts of the sound-speed profile with high relative curvature $U_{10}(z)$ are labeled with "FS." At these depths, U_{10} is equal to 5.7, 5.7, and 5.8 for T1, T2, and T3, respectively, which is greater than 95% of the relative curvatures (not shown) between 0 and 200 m depth in each profile. The depth-mean U_{10} for sound-speed profiles during T1, T2, and T3 is 3.9, 3.9, and 4.1, respectively. According to previous studies, the mean relative curvature of these profiles is large enough to expect multiple ray triplications.

Vertical fine-scale structures were frequently observed from depths of 50–150 m during the experiment from other oceanographic instruments. A vertical auto-correlation function of sound speed was calculated between depths from 50 to 150 m using sound-speed profiles from four nearby Wire Walkers. The average scale of the fine structure was 7 m, which is the vertical lag necessary to reduce the vertical auto-correlation function to half its value. The auto-correlation function of the first derivative of sound speed was estimated by multiplying the Fourier transform of the auto-correlation function by a factor of k^2, the vertical wavelength, and then inverse-transforming the product. The result had a vertical decorrelation of 1.2 m. This decorrelation suggests the second-derivative-length scale can be on the order of a meter or less.

The displacement of the sound-speed profile by internal waves is shown in Fig. 5 with a series of minute-interpolated sound-speed profiles stacked next to each other over a period of roughly 2.5 h centered around transmission T2. The changing position of the fine structure over time (e.g., the curvature in the sound-speed profile between 95 and 100 m) and the motion of potential isotherms of 9.2, 10.8, and 11.4 °C with mean depths of 83, 118, and 130 m highlight the vertical motion of the internal waves. The vertical displacement of the fine structure near 120 m depth is estimated by the change in depth of the 10.8° isotherm (green line). The isotherm depth deviated from a mean depth of 118 m by ±4 m over the 2.5-h period with a 1.8 m standard deviation. On 17 May from 19:10 to 19:20, the 10.8° isotherm was displaced upwards by one meter. The gradients of the fine structure at the 10.8° isotherm depth are vertically displaced by one meter as well over this period. The displacement of the fine structure perturbs two acoustic receptions. These receptions are discussed further in Sec. V.

In addition to the vertical displacement of internal waves, on-isopycnal variability of salinity and temperature creates lateral changes in the sound-speed profile. This variability, referred to as spice, corresponds with temperature variability that compensates for the salinity-related changes in density on an isopycnal. The total sound-speed anomaly can be decomposed into two components: vertical displacement of isopycnals and the spice anomaly along isopycnals.[27] The on-isopycnal variability in the California Current System, in general, is due to larger-scale oceanographic processes related to water mass formation and mixing.[28] The interleaving of different water masses can contribute to vertical sound-speed gradients. However, the horizontal advection of these water masses is not changing the sound speed at time scales comparable to the displacement from internal waves, see Fig. 6(a). Hence, we focus on the vertical displacement of the isopycnals from internal waves, specifically near the turning point of the transmission, as the dominant oceanographic process contributing to the acoustic fluctuations.

An 11 km transect during a four-hour period of FastCTD profiling on 18 May from 7:30 to 11:30 is used to quantify the relationship between temperature and salinity in the region, see Fig. 6(b). The temperature, salinity, and pressure measurements from the FastCTD are plotted with labeled contours of density shown at 0.2 kg/m^3 intervals. The mean and standard deviation of salinity and temperature (black line with cross-marks) are interpolated to form the empirical salinity-temperature relationship $S(T)$. The sound-speed anomaly along three isopycnals during the transect with mean depths of 60, 100, and 140 m shows the lateral scale of the spice anomaly, see Fig. 6(a). The sound speed along isopycnals (green and yellow lines) near the turning depths of the ray paths in the experiment changed on the order of 1 m/s over roughly 10 km. The isopycnal near the mixed layer (red line) changed 2 m/s over roughly 1 km due to the distinct water masses on the 1024.8 isopycnal, see Fig. 6(b).

The empirical salinity-temperature relationship shown in Fig. 6(b) is used to estimate the salinity from thermistor temperature. Relating salinity to temperature is necessary to calculate the sound speed which depends on both variables. However, the sound-speed equation of state c_{eos} is weakly dependent on the salinity, hence the contribution from the error in estimating salinity to the error in estimating sound speed is small. For example, the error made between a sample salinity on the 1025.2 kg/m^3 isopycnal and the estimated salinity using the empirical salinity-temperature relationship evaluated at the sample temperature is at worst 0.085 PSU.

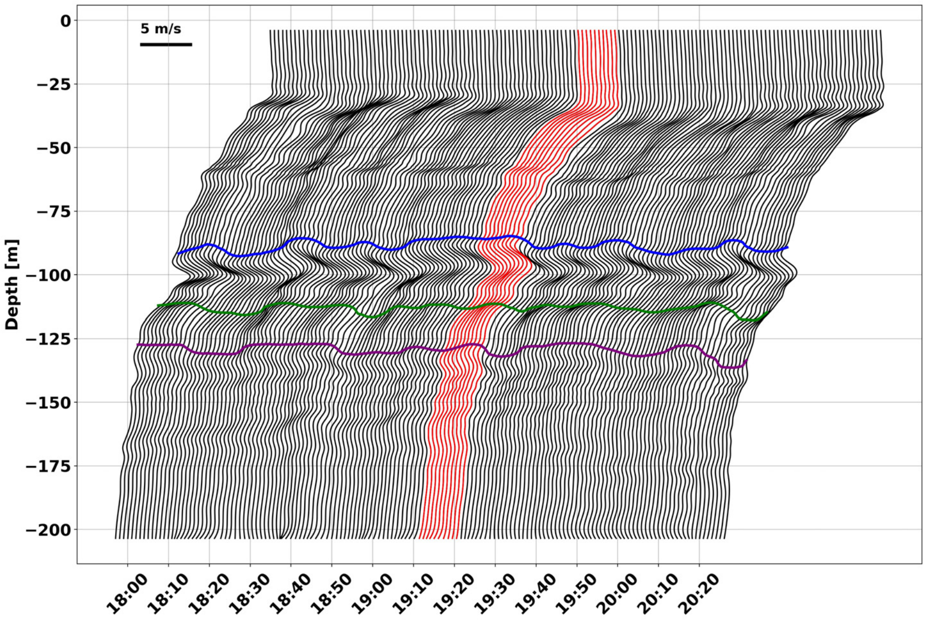

FIG. 5. (Color online) A series of interpolated sound-speed profiles using estimates from the drifting thermistor chain (TC5) plotted roughly over 2.5 h on 17 May from 18:00 to 20:30 during the T2 transmission. The sound-speed profile at minute 19:10 is shown in Fig. 4(b). Each profile is separated by one minute in time. Time and sound speed is plotted on the same axis, and so the 5 m/s scale bar at the top left helps show the scale of the sound-speed profiles. The time of each profile is aligned with the time axis starting at the bottom of each profile. Three colored lines show constant potential temperature contours of 11.4 °C (blue), 10.8 °C (green), and 9.2 °C (purple). The red sound-speed profiles highlight a 10-min period that is related to acoustic receptions discussed further in Sec. V.

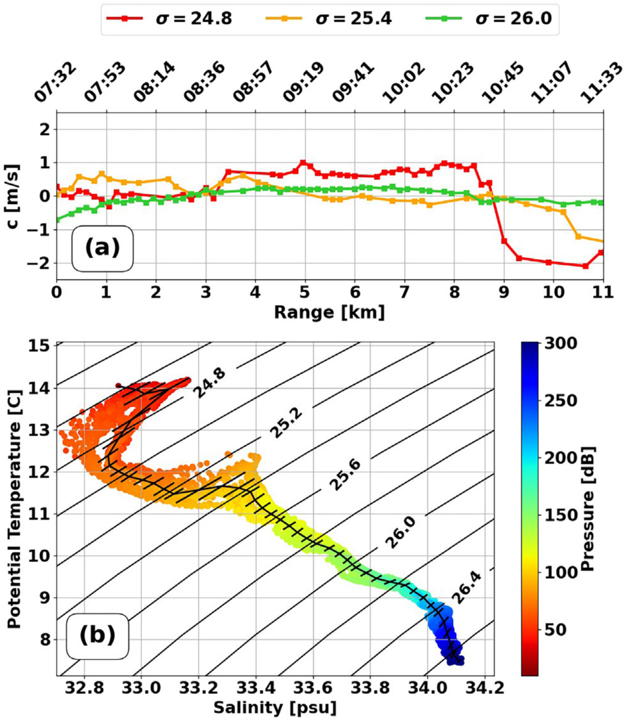

FIG. 6. (Color online) Salinity, temperature, pressure, and density measurements from 3-min sampled FastCTD profiles down to 300 m depth during a four-hour transect on 18 May. (a) The sound-speed anomaly from the mean sound speed along an isopycnal over the transect for densities of 1024.8, 1025.4, and 1026 kg/m^3 with mean depths of 60, 100, and 140 m. (b) Salinity and temperature measurements (colored dots) with contours of constant density (labeled black lines) plotted at 0.2 kg/m^3 intervals. The pressure of each sample is shown in color. The mean temperature and salinity curve is calculated from 1024.6 to 1026.6 kg/m^3 at intervals of 0.05 kg/m^3 and is plotted in (b) as a black line with cross-bars that represent the standard deviation of temperature and salinity within each density interval.

This deviation in salinity contributed at most 0.1 m/s error to the sound-speed estimate, which was less than or equal to other uncertainties. The root mean square error of sound speed from the error in salinity is 0.03 m/s.

B. Acoustic observations

Over various short-range acoustic transmissions during the experiment, the matched-filtered sequences had between two and four arrivals from refracted ray paths at ranges of less than 3 km at a source depth of 200 ± 4 m. Figures 7(a), 7(c), and 7(e) show the intensity of recorded acoustic arrivals from single matched-filtered sequences over the entire receiver array near the middle of the transmission intervals T1, T2, and T3. Figures 7(b), 7(d), and 7(f) show a series of arrivals from multiple matched-filtered sequences on single hydrophones during the minute-long transmission of T1, T2, and T3. The display of arrivals in the left column is generally referred to as a timefront with each separate line of arrivals referred to as a branch. The observed timefront contained multiple branches separated within milliseconds of each other and a longer-delayed branch that likely was reflected from the surface. This paper focuses on the refracted arrival branches that do not scatter off the surface. Only a single matched-filtered sequence over the array is shown in Figs. 7(a), 7(c), and 7(e) because the shape of the observed timefronts did not vary much over each one-minute transmission interval, however, the location of the timefront with respect to arrival time and depth does vary slightly due to the small changes in source depth and transmission range.

During transmission T1, shown in Fig. 7(a), the array received two refracted arrivals and one surface-reflected arrival from the source at a range of 1.7 km. The first two refracted arrivals R1 and R2 had a time separation of 1.5 ms. The time separation between the two arrivals is smaller at the top of the array than at the bottom suggesting a difference in their angle of arrival at the receiver. During transmission T2, shown in Fig. 7(c), the array also received two refracted arrivals and one surface-reflected arrival at a range of 1.9 km. These arrivals were similar to the arrivals in T1, although, R1 and R2 overlapped at a depth of 130 m near the top half of the array. The intensity of the arrival appears to increase where R1 and R2 overlapped. During transmission T3, shown in Fig. 7(e), the array received 4 arrivals, three refracted and one surface reflected, at a range of 2.5 km. Arrivals R1 and R2 overlapped at multiple locations. Arrival R3 did not overlap with the first two. It is possible that R3 is two interfering paths because R3 temporarily appears to split, at geophysical time 32 s and arrival time 10 ms, into two smaller arrivals, see Fig. 7(f). Arrivals shown in Figs. 7(a), 7(c), and 7(e) are attributed to ray triplications which allow for the arrivals to have small time separations.

The arrival intensity structure along the array, shown in Figs. 7(a), 7(c), and 7(e), is projected into the temporal variability of arrival intensity recorded on a single hydrophone, shown in Figs. 7(b), 7(d), and 7(f). The rapid changes seen in the time evolution of the refracted arrivals during T3, Fig. 7(f), can be explained by the overlapping arrivals seen along the timefront in Fig. 7(e) sweeping across a single hydrophone over time. The surface waves—which were particularly strong during T3—caused the ship to heave resulting in the source depth changing by ±4 m with a period of ≈7 s. Ray simulations showed that an upwards source motion shifts the arrival depth of a triplication downwards, and conversely shifts the triplication upwards for a downwards source motion. The pattern of intensity along the time front [Fig. 7(e)] is visible in the time record in Fig. 7(f) as a series of interleaving paths due to the motion of the acoustic source. This effect can be removed by sampling transmissions that had the same source depth, but the effect illustrates how structure along the timefront can impact the time series of arrivals for a single hydrophone.

IV. MODEL

A. Ray triplication/wavefront folding

A ray model illustrates the change in acoustic propagation due to the sound-speed fine structure. A two-dimensional (r,z) range-independent ray trace is simulated

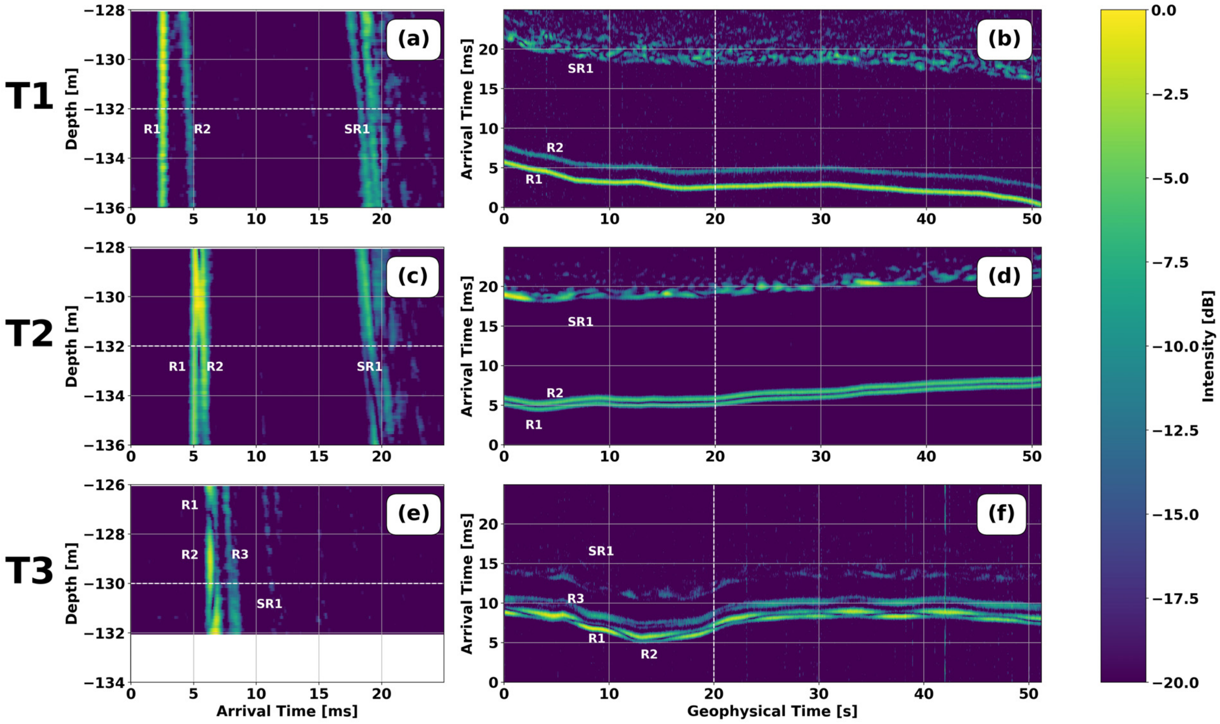

FIG. 7. (Color online) Observed matched-filtered acoustic arrivals on different days with varying ranges between 1.7 and 2.5 km. (b), (d), (f) The geophysical time evolution of arrivals for T1, T2, and T3 over one minute with the arrival intensity shown in color and the relative arrival time on the vertical axis for a single hydrophone centered in the middle of the array shown as the horizontal white dashed line on the left column. The arrival intensity is relative to the maximum arrival intensity recorded on the array for each snapshot and is reported in decibels. (a), (c), (e) The arrival intensity for T1, T2, and T3 in color with the relative arrival time on the horizontal axis and hydrophone depth on the vertical axis for a single transmission at the time marked by the vertical dashed line on the right column. Each transmission contained multiple arrivals labeled with an "R" for a refracted and an "SR" for a surface reflected. The bottom 16 hydrophones in the array lost power during T3, and so there is a blank space in (e) where no data is available at those depths.

using a sound-speed profile from T1, see Fig. 8(a), which is the same sound-speed profile shown in Fig. 4(a). Rays were traced at constant launch angle increments of 0.05° over a range of 1.8 km, shown in Fig. 8(b). Ray angles throughout the ray trajectory are defined from the horizontal axis with rays approaching the surface having positive ray angles and rays approaching the bottom with negative ray angles.

Caustics form when the spatial separation between two rays, separated by an infinitesimally small launch angle, decreases to zero.[29] Rays near a caustic crossover each other creating a triplication, see the upper left corner of Fig. 8(b). Caustics occur at the folding points of timefronts, where $dz_f/d\theta_0$, the derivative of ray depth at the range of the receiver, z_f, with respect to the launch angle θ_0, changes sign.[30] The color of the rays in Figs. 8(b) and 8(c) changes when $dz_f/d\theta_0$ changes sign. The ray arrivals at a 1.8 km range in Fig. 8(c) contain two triplications near 60 and 110 m depth. These triplications stem from rays with turning points between 50 and 60 m and 90–120 m depth. At 55 and 100 m depth, U_{10} is 5.1 and 5.8, respectively. The relative curvature at these depths is sufficient to form triplications for rays with nearby turning points.

The ray arrivals related to the triplication near 110 m form a swallow-tail pattern, see inset plot of Fig. 8(c). The three branches B1, B2, and B3 of the triplication are labeled in Fig. 8(c). Branch B1 (magenta rays) consists of rays with positive angles with an average of 1°. The arrival angle of rays along the triplication goes through zero at the top of the triplication where Branches B1 and B2 connect. The ray angles on B2 (red rays) are negative with an average of −3.3°. Ray angles on Branch B3 (teal rays) increase slightly after passing through the bottom of the triplication and have an average angle of −3.0°. Branch B3 has the lowest intensity of the three branches as seen by the increase in spacing between ray arrivals, and the ray angles are very similar to Branch B2. Branch B3 might not be resolved in the observations for those two reasons. Arrivals from triplicated ray paths plausibly explain observations of closely separated and overlapping arrivals with varying intensities.

The formation of the triplication related to the arrivals near 110 m depth starts near the caustic between 1200 and 1800 m in range and 90–120 m in depth which is shown in the upper left corner of Fig. 8(b). Figures 9(a), 9(b) focus further on the area where the wavefront starts to fold due to the fine structure at those depths. Figure 9(a) shows the value (black line), first (blue line), and second (green line) derivative of the interpolated sound-speed profile between 92 and 105 m depth. The propagation of the simulated wavefront, curves in r, z space of constant travel time, is shown in Fig. 9(b) between 1450 and 1600 m in range by 92–105 m in depth. Each wavefront is sampled every 10 ms in travel time starting at a relative initial travel time of 0 ms. The range variability along each wavefront is a few centimeters, whereas the range separation between each wavefront is

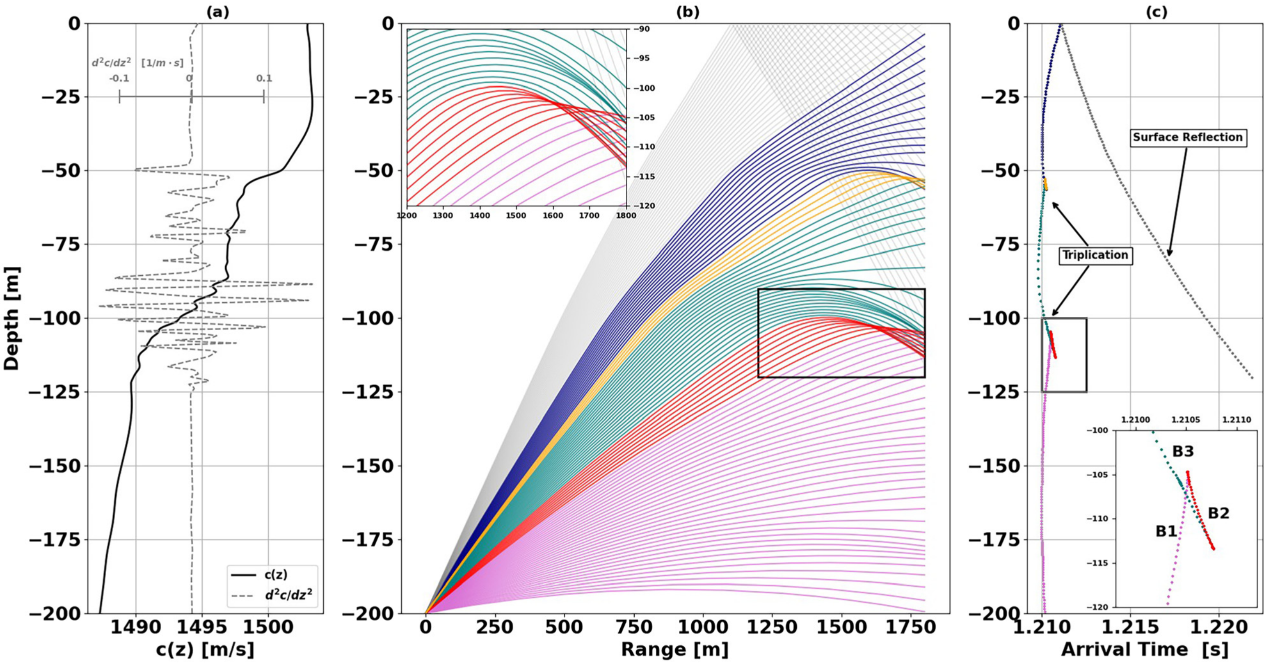

FIG. 8. (Color online) A ray trace simulation using the sound-speed profile from T1 is shown in Fig. 4 and redrawn in (a) (black line) in combination with the second derivative in sound speed (gray line). (b) A ray trace over 1.8 km with an inset plot that focuses on rays forming a triplication. Ray bundles, highlighted with different colors in (b), are delineated by the change in sign of the derivative of ray arrival depth with respect to launch angle, $dz_f/d\theta_0$. The rays that are reflected from the surface are shaded in light gray. The inset plot in (b) focuses on rays that pass through caustics and continue to crossover each other. (c) The ray arrival time versus ray arrival depth at a 1.8 km range. The inset plot in (c) focuses on the triplication area near 110 m. Each branch of the triplication in the inset plot is labeled B1, B2, and B3.

15 m. The mean range separation between each wavefront in Fig. 9(b) is reduced from 15 m to 5 cm to emphasize the along-wavefront variability relevant to triplications.

The wavefront begins converging near depths of 94, 98, and 104 m. At these depths, the second derivative of sound speed [Fig. 9(a) green line] has negative extrema, which cause the rays in the vicinity of these depths to progressively squeeze together. The wavefront near 100 m depth and 40 ms travel time converges to a focal point (caustic), after which the wavefront folds over itself. The wavefront tends to fold in areas where the rays are near horizontal, so the wavefront is aligned vertically, making it more sensitive to the vertical changes in the sound-speed profile.[13] The curve $r(z)$ that describes the wavefront range as a function of depth is multi-valued across the fold. The colors of the wavefront in Fig. 9(b) correspond to the three branches of the triplication

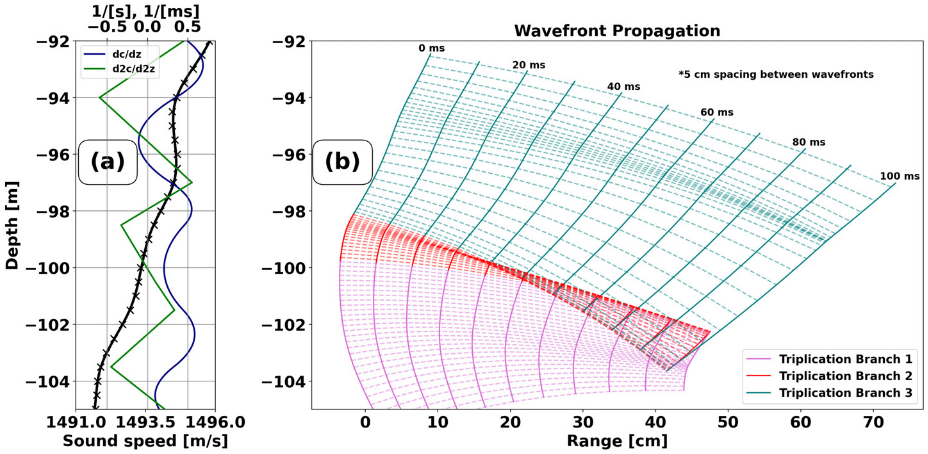

FIG. 9. (Color online) (a) An example sound-speed profile between 92 and 105 m, shown on the left side (black solid line), contains multiple "step-like" structures that have non-trivial second derivatives (green solid line) in sound speed with respect to depth by alternating the first derivative in sound speed (blue solid line). (b) Wavefronts at 10 ms travel time intervals are calculated from simulated rays between ranges of 1450 and 1600 m. Solid lines represent the wavefront, a curve of constant travel time, and the dashed lines which represent acoustic rays. The mean range separation between each wavefront is re-scaled from 15 m to 5 cm to emphasize the curvature along the wavefront. The wavefront folds over itself as it propagates which forms a triplication near 102 m depth. The colors magenta, red, and teal each represent a different branch of the triplication for the wavefront with a 100 ms travel time.

shown in Fig. 8(c). From the ray point of view, the folding of the front involves neighboring rays crossing over each other, allowing for three rays with distinct travel times to occupy the same point in space where the wavefront has folded.

This fold shown in both the wavefront, shown in Fig. 9(b), and in the timefront, shown in the inset plot of Fig. 8(c), demonstrates how ocean fine structure allows for distinct ray paths that have small vertical separation while still arriving at the same depth at short ranges. For example, rays on branches B1, B2, and B3 that intersect 110 m depth at a range of 1.8 km had maximum vertical separations of 12, 19, and 9 m between their respective rays paths at a range of 1.5 km where the rays on branches B2 and B3 start to turn.

B. Model comparison

The PE model is compared to the ray model by overlaying ray arrivals on top of the PE simulated intensity shown in Fig. 10 for each transmission. Both simulations used the estimated transmission ranges, source depths, and sound-speed profiles from the three transmission periods, see Fig. 7. The PE simulations used the spectral shape of the pulses sent during the experiment. Figures 10(b), 10(d), and 10(f) show simulated acoustic receptions that have the same pulse shape, source depth, and range as the simulated receptions shown in Figs. 10(a), 10(c), and 10(e), but use sound-speed profiles smoothed by convolving a 12-meter boxcar window with the interpolated sound-speed profiles for T1, T2, and T3. Smoothing the sound-speed profile of T1, T2, and T3 decreases the depth-mean U_{10} of each profile down to 2.9, 2.8, and 3.0, respectively. Figures 10(b), 10(d), and 10(f) show the change in PE and ray timefront when the fine structure is removed by smoothing. To further quantify the effect of smoothing the sound-speed profile, this smoothing technique is applied to the interpolated sound-speed profiles with various window lengths and the resulting simulated propagation is compared to the observations in Sec. V.

The intensity along the ray timefront can be estimated from the arrival depth separation between successive rays because the rays have uniform increments in launch angle. Each transmission has at least two branches of arrivals. Branches that reflected from the surface are labeled "SR," and branches that were wholly refracted are labeled with "R." Along each refracted branch there are in general extra branches that are created by the ray triplication process. Simulated arrival branches that are associated with the observed arrivals are labeled the same as in Fig. 7. Not all the branches can be associated with the observations because the aperture of the array, see Fig. 7(a), is small compared to the depth range of the simulated timefront. The overall structure of the PE and ray timefront tend to agree, although, in some areas, PE simulated energy appears where the rays are shadowed, e.g., Fig. 10(a) between 125 and 150 m.

Figures 10(a), 10(c), and 10(e) show simulated output using unsmoothed sound-speed profiles for transmissions T1, T2, and T3, which are ordered by increasing range. T1 appeared to have the least amount of complexity in the timefront, based on the number of branches and the intensity variability, while T3 had the most. Timefront complexity thus increased with range, as might be expected. T1 and T2 show branches, e.g., R2, extending from ray triplications near depths of 50, 100, and 125 m. The strong sound-speed gradient at the base of the mixed layer, see Fig. 4(c), during transmission T3 explains the discontinuity between 25 and 50 m depth and additional arrival branch, R3, in the timefront shown in Fig. 10(e), that do not occur in the T1 or T2 timefront.

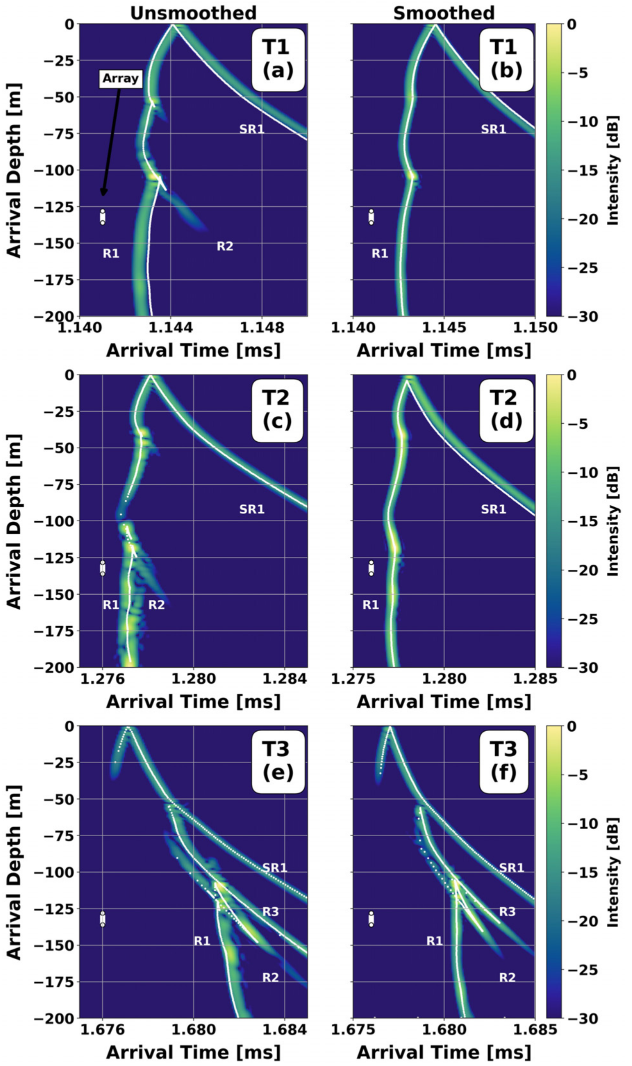

FIG. 10. (Color online) Three simulated acoustic arrivals using sound-speed estimates shown in Fig. 4 with and without sound-speed smoothing. (a), (c), (e) The simulation of transmission T1, T2, and T3 at ranges of 1.7, 1.9, and 2.5 km, respectively, without any smoothing to the sound-speed profiles. (b), (d), (f) The simulations in (a), (c), (e) with a 12 m smoothing window applied to the sound-speed profile. Intensity calculated by the PE simulation is shown relative to the maximum arrival intensity in decibels with color. Ray arrivals are shown as white dots. Each branch of the timefront observed by the receiver is labeled with the same arrival labels in Fig. 7. The scale and depth of the experimental array aperture are shown in each figure on the left-hand side between depths of approximately 128–136 m.

The change in acoustic amplitude described by the ray model is governed by the convergence and divergence of the ray tube which depends on the second derivative of sound speed along the ray path.[30,31] Areas of high intensity appear near points where the timefront splits into two arrival branches, e.g., near 110 m between R1 and R2 in Fig. 10(a). This split is the top part of the triplication shown in Fig. 8(c). This area of high intensity is associated with a caustic. The simulated arrivals retain areas of high intensity at depths where the unsmoothed simulated timefront folds over because the second derivative of sound speed in those areas is strong enough to significantly focus the acoustic energy, even after smoothing.

The PE and ray simulations tend to agree on the location of caustics along the timefront, however, the PE simulations show energy extending from the caustics in the timefront which are not paired with ray arrivals. This is most clear for the caustic in Fig. 10(a) near 110 m depth. Both ray and PE simulated receptions show a second arrival branch, R2, in the timefront underneath the caustic. R2 calculated from geometric ray tracing terminates at a depth of 112 m whereas R2 calculated with a full-wave PE simulation extends to a depth of 140 m. This extension of energy is asymmetric with more energy scattered below than above the triplication. The ray trace does not model the extension of energy but does predict areas of triplication that appear to be the source of this extension.

The PE model includes information about the acoustic wavelengths within the bandwidth of the experimental transmissions, and models wave scattering when the wavelength is comparable to or larger than the length scale of the changes in sound speed. Hence, when the sound-speed profiles are smoothed with a 12 m window length, the PE simulated transmission of T1 and T2 lose their R2 arrival branches, and the energy below 125 m for T2 and T3 appears less scattered across the timefront because the vertical length scales of the sound-speed profiles are increased by smoothing. The vertical Fresnel zone, $R_f \approx 1/2\left(\sqrt{\lambda R}\right)$, can quantify the acoustic sensitivity to vertical scales in the sound-speed profile.[30] The vertical Fresnel zone for ray paths connected to arrivals R1 and R2 is approximately 10 to 20 m based on the bandwidth of the pulses. This calculation assumes a free-space medium and the curvature of the waveguide can make the Fresnel zones much smaller.[30]

V. RESULTS

A. Model-observation comparison: Intensity

A deterministic comparison was made between arrivals observed over the array and PE simulations of arrivals for each of the three transmission periods. Figure 11 compares the intensity of the observed and simulated pulses. The intensities are shown in decibels in Fig. 11 and are relative to the maximum arrival intensity recorded on the array during the snapshot. Figures 11(a), 11(c), and 11(e) show a snapshot of a single pulse arrival [expanded view of Fig. 7(a), 7(c), and 7(e)] within the same minute interval as the simulated result shown in Figs. 11(b), 11(d), and 11(f). The range of the transmission can be estimated with the measured travel time and sound speed but has an uncertainty of roughly 30 cm. A single travel time offset is used to align the observed and simulated timefronts along the center of the time delay axis. These comparisons show good visual agreement demonstrating that the closely spaced arrivals observed during the experiment were consistent with ray triplication created by oceanographic fine structure in the sound-speed profile.

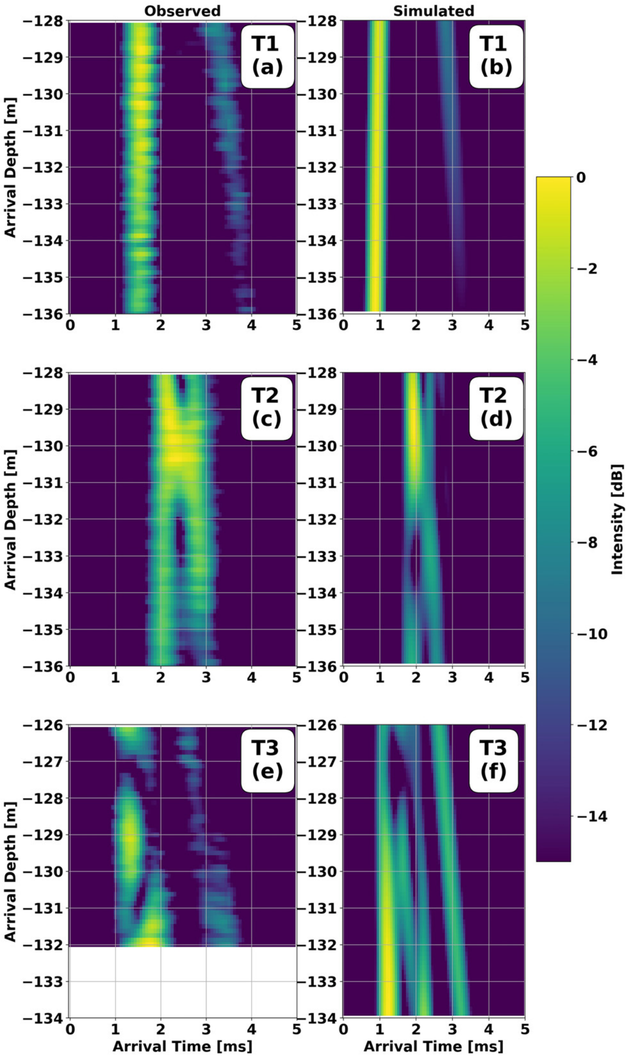

FIG. 11. (Color online) Three snapshots of observed pulses from the experiment (left column), and modeled pulse propagation (right column) using sound-speed profiles within 2 km. (a), (b) Observed and simulated arrivals from T1; (c), (d) T2; (e), (f) T3. The intensity of arrivals relative to the maximum arrival intensity is shown in decibels with color over the 7.875 m array aperture for an arrival time window of 5 ms. The arrivals are centered in each plot, with the travel times adjusted to match because of the uncertainty in the transmission range.

The interpolated profiles in Figs. 4(a), 4(b), and 4(c) and the measured source-receiver geometry were used to make a set of baseline PE simulations, see Figs. 11(b), 11(d), and 11(f), for each transmission. Another set of simulations was made with perturbations to the range, source depth, and sound-speed profile. The simulations, perturbed and unperturbed, were compared to the observed intensity along the array with a correlation, r, a skill score, SS, and

TABLE I. Values of the correlation, r, skill score, SS, and relative mean squared error, MSE_r, quantify the difference between the observed and simulated arrival amplitudes. The rows in the leftmost column dictate the type of perturbation made to the simulation's parameters. Each column corresponds to a transmission with sub-columns for each metric. The unperturbed row uses the range, source depth, and sound-speed profile that best match the acoustic transmission. The range and source depth of the simulations were perturbed and their agreement with the observations is reported in the middle rows. Simulations using sound-speed profiles measured farther away from the turning point of the acoustic path are available for two transmissions. Comparisons between observations and those simulations are listed in the last row.

	T1			T2			T3		
Perturbation	r [%]	SS [%]	MSE_r [dB]	r [%]	SS [%]	MSE_r [dB]	r [%]	SS [%]	MSE_r [dB]
Unperturbed	93	80	–24.17	90	80	–23.32	72	64	–19.73
Range + 50 m	90	80	–23.48	88	74	–22.56	59	48	–17.72
Range –50 m	93	76	–23.37	88	71	–22.26	62	56	–18.62
Source depth + 3 m	93	79	–23.77	88	74	–22.44	49	42	–16.72
Source depth –3 m	92	79	–24.07	89	76	–22.54	70	64	–19.56
Alternative profile	83	58	–21.60	—	—	—	50	28	–16.24

mean squared error relative to noise, MSE_r, see Table I. The r value measures the correlation between the amplitudes, which is less sensitive to the difference in magnitude between two received pulses than to the difference in pulse shape, whereas the skill score and MSE_r are sensitive to the difference in the magnitude and shape between the received pulses, and has a larger range of values over the set of comparisons. These metrics quantify the importance of each parameter to the difference between observed and simulated arrival amplitudes. The Appendix describes how these metrics are computed from the data.

In general, the PE simulations using a well-resolved sound-speed profile near the turning point and the correct acoustic parameters predicted the number of observed arrivals and replicated the relative travel time separation between those arrivals. The variation in intensity along each arrival branch was not as well replicated in the simulations shown by the lower values of skill score compared to the correlation. The agreement between the observed and simulated intensity was more sensitive to changes in the sound-speed profile than to small changes in the range or source depth. The last row of Table I uses sound-speed profiles made solely from the thermistor-chain measurements, shown in Figs. 4(a) and 4(c), without supplemental measurements from the Wave Glider. The simulations in the first row of Table I used sound-speed measurements from the Wave Glider which were made at the turning point depth and roughly 100 m and 2 km away from the turning points in range during T1 and T3, respectively. The correlation between observation and simulation decreased by 11% for T1 and 30% for T3 when solely using the thermistor-chain measurements at the turning point depths. The thermistor measurements were 1.5 km and 4 km, respectively, away from the turning point in range. The decrease in correlation emphasizes the importance of measuring the sound-speed profile near the turning point of the acoustic transmission.

In another perturbation experiment, the sound-speed profile closest to the turning point was smoothed by convolving a boxcar window with the profile for window lengths of 2, 4, 8, 12, and 20 m. The sensitivity simulation indicated that modifying the sound-speed profile by vertical smoothing reduced the number of arrivals overall, decreasing both the correlation and skill score, see Fig. 12. The correlation is not as sensitive as the skill score and flattens off after a smoothing window length of 8 m. The skill score decreased monotonically as the sound-speed profile smoothing window length increased. The decrease in skill score between 0 and 2 m window length is smaller than 2 to 4 m window length, indicating structures under 4 m need to be resolved in the sound-speed profile in order to adequately match the simulated pulses to observations, although higher resolution improves the match.

The drifting nature of the experiment made it difficult to position the oceanographic platforms so that they could measure the range variability along the acoustic propagation path. The agreement between our range-independent simulations and the acoustic observations gives us confidence that our range-independent assumption is reasonable. Additionally, two range-dependent environments were made to test the sensitivity of the simulated propagation to horizontal sound-speed variability. Lacking horizontally separated sound-speed measurements along the transmission path between the source and receiver, we convert hour-long and 30-min-long time series of sound-speed profiles, see Fig. 5, centered on Transmission T2 into a spatial series by spacing each profile in range by a fixed distance.

The 30-min and hour-long series separate consecutive profiles in range by 67 and 33 m respectively. These range-dependent simulations test cases where the range dependence of the sound channel is strong. The ratio between the spatial to temporal decorrelation scale of the sound speed, approximately 4 km per 24 min, would suggest a profile every 167 m. Even with 67 and 33 m horizontal separations, adding horizontal range dependence to the simulation did not greatly affect the arrivals at the 1.9 km range. The hour-long series was 92% correlated with the range-independent simulation. The 30-min-long series was 95% correlated with the range-independent simulation. Neither of the range-dependent simulations increased the agreement between observation and simulation which is expected since the range-dependent simulations do not have the true range dependence for those transmissions.

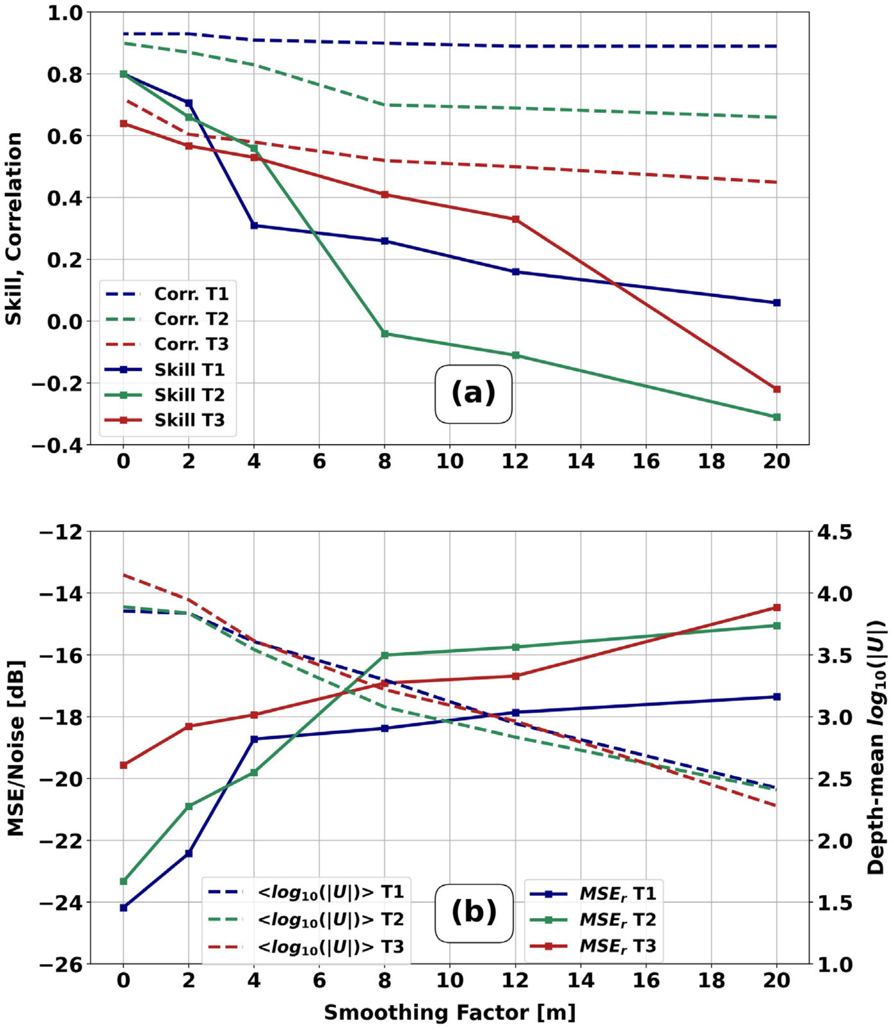

FIG. 12. (Color online) Values of skill score (solid line) and correlation (dashed line) between observation and simulation for the three transmissions T1 (blue line), T2 (green line), T3 (red line) as a function of window length (smoothing factor) used to smooth the sound-speed profile are plotted in (a) (top). The mean-squared error between observation and simulation divided by the squared amplitude of the observed noise in decibels (solid lines) and the depth-mean $log_{10}(|U(z)|)$ of the sound-speed profile (dashed lines) for T1 (blue line), T2 (green line), T3 (red line) are plotted as a function of the window length used to smooth the sound-speed profile in (b) (bottom).

B. Model-observation comparison: Phase

The phases of the 4 kHz carrier frequency along the array for a single MLS transmission in the middle of the minute-long series from the observations, see Fig. 13(a), 13(c), and 13(e), were computed from the output of the matched filter on the demodulated receptions.[16] The phases of the simulated propagation, see Figs. 13(b), 13(d), and 13(f), were evaluated as the angle between the complex components of the baseband pulse. Values that have lower than –15 dB intensity are not shown in the figures. It is not possible to compare the absolute phase between the simulation and observation because the range uncertainty is greater than 30 cm, which is the amount of range required to change the phase by 1 cycle. A single phase offset is added to the simulated phase so that it is easier to compare the simulated to the observed phase along each arrival depth.

The angle of arrival, θ, of the wavefront with respect to the array is estimated using both the rate of change in phase and travel time over the vertical span of the array. The estimated angle of arrival, $\hat{\theta}_\tau$ and $\hat{\theta}_\phi$, is congruent to the ray angle defined by the ray coordinate system. The travel time and phase are evaluated at the peak values of the received arrival amplitude. These peaks are shown as circles in Fig. 13. A line is fit to peak phase and travel time measurements and the slope is used to estimate the rate of change in both quantities along the array. Equation (2),

$$\hat{\theta}_\tau = \tan^{-1}\left(\left[\frac{d\tau}{dz}\right]c\right), \tag{2}$$

is used to estimate angle $\hat{\theta}_\tau$ with travel time where $d\tau/dz$ is the change in arrival time with respect to depth, and c is the local sound speed. Equation (3),

$$\hat{\theta}_\phi = \tan^{-1}\left(\left[\frac{d\phi}{dz}\right]\frac{c}{\omega}\right), \tag{3}$$

is used to estimate angle $\hat{\theta}_\phi$ with phase where $d\phi/dz$ is the phase rate with respect to depth, ω is the angular frequency, and c is the local sound speed.

The angle of arrival estimates are reported in Table II. The difference between observed and simulated arrival estimates is at most a few degrees, which demonstrates the capability of the simulation to accurately represent the phase distribution over the array. The average difference between observation and simulation angle estimates using travel time

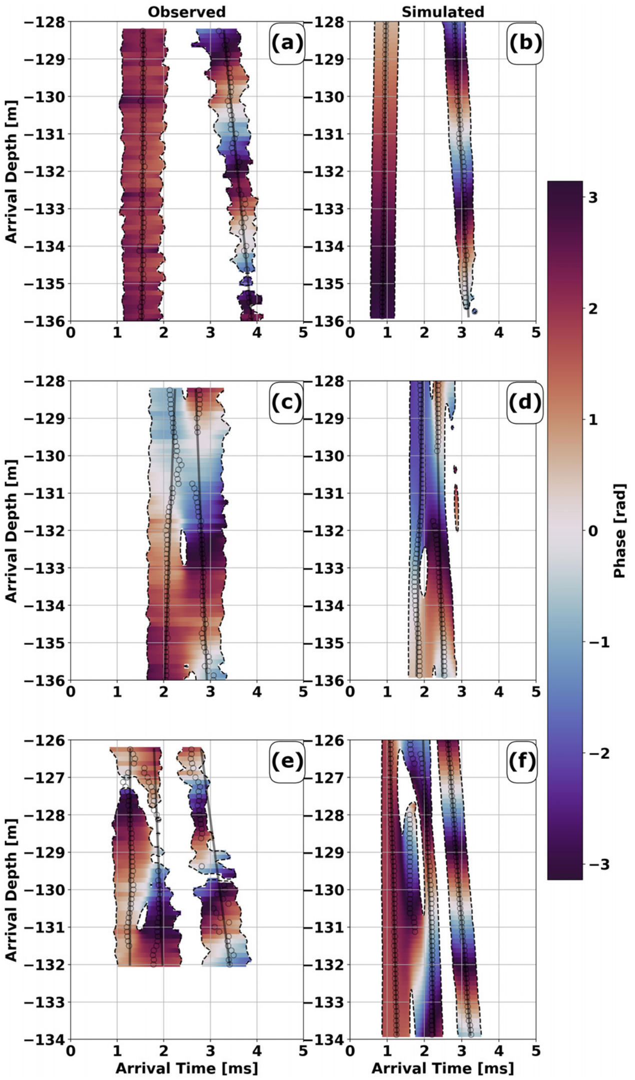

FIG. 13. (Color online) A comparison between observed and simulated arrival phase. Arrival phases that have an arrival intensity of –15 dB less than the maximal arrival peak are not shown. (a), (c),(e) The observed carrier phases along the array for a single transmission during T1, T2, and T3 respectively. (b),(d),(f) The simulated carrier phases of transmissions T1, T2, and T3 with a single phase offset allowed to ease the comparison between observed and simulated phases. Circle markers show the location of peak intensities of each arrival with the solid lines showing a linear fit to those peak arrival times along the vertical axis.

was 1° and using phase was 1.6°. Differences were greatest for T3 and least for T1 as expected. The overlap of arrivals for both T2 and T3 leads to some disagreement between the phase and travel time angle estimate. For example, the phase estimate of the second arrival angle for T2 differs by 1.9° from the travel time estimate of the arrival angle. When two pulses overlap in arrival time the phase underneath the envelope of the overlapping pulses is affected by both the phase and amplitude of the two pulses. This interference can cause the phase to deviate from a constant rate of phase change along the array. The overlapping of arrivals can also change the envelope shape, therefore, adding uncertainty to the travel time estimate of the arrival angle, but to a lesser extent than for the phase estimate.

TABLE II. Estimated arrival angles for different transmissions T1, T2, and T3 for both observations (DATA) and simulations (SIM) are reported in each row. The left half of the table shows the travel time estimates of arrival angles. The right half shows the phase estimates of arrival angles. Each column delineates the arrival numbers which are ordered by the time of arrival. A dashed line in the table means that particular arrival was not received during the transmission.

	Arrival Angle					
	Travel Time Estimate			Phase Estimate		
Transmission	1st	2nd	3rd	1st	2nd	3rd
T1 (DATA)	0.35°	−6.6°	—	0.42°	−6.2°	—
T1 (SIM)	1.18°	−5.3°	—	1.18°	−4.9°	—
T2 (DATA)	2.7°	−3.3°	—	1.7°	−3.7°	—
T2 (SIM)	1.7°	−3.5°	—	1.4°	−1.8°	—
T3 (DATA)	0.1°	−2.7°	−9.1°	−4.3°	−3.8°	−9.4°
T3 (SIM)	0.5°	−3.8°	−6.4°	−0.6°	−5.1°	−6.8°

The ray trace using the sound-speed profile from T1 predicted a single arrival at the depth of the array. The PE simulation correctly models the energy that was received on the array during T1 with an estimated arrival angle within a degree of the observed arrival angle. Branch 2 of the triplication, shown in Fig. 8(c), is connected to the extension of energy, shown in Fig. 10(a). In the ray trace, Branch 2 has a −3.3° arrival angle whereas the estimated angle from the observation was −6.6°. The angle of the received wavefront from the caustic extension must steepen as it reaches the depth of the array, which would explain the discrepancy between the observed arrival angle and ray angle.

C. Time evolving amplitude comparison

A longer time series of acoustic arrivals during T2 was processed to compare the evolution of the arrivals over a few minutes to a simulated evolution. Figure 14 shows a 10-min record during T2 starting on 17 May 19:10 on a hydrophone at 129 m depth, which is above the interference of two arrivals shown in Fig. 7(d). Figure 14(a) shows all of the arrivals including the surface arrival. The travel time of arrivals in Fig. 14(a) vary due to the varying range between the drifting array and the shipboard source. The range between source and receiver increased by 30 m over the 10-min period on 17 May from 19:10 to 19:20. The relative time delay between surface and refracted arrivals was roughly constant over the 10-min record which suggested the change in travel time could be corrected with a single time delay adjustment for each MLS reception.

The change in the arrivals due to sound-speed changes was isolated by removing the travel time effect of range and filtering for source and receiver depth changes within half a meter. A time-lag cross correlation was calculated between the intensity of the two refracted arrivals from each reception and the intensity of the two refracted arrivals from the previous reception. The time lag with maximal cross correlation estimates the change in travel time from one reception to the next. Those time-lags were then used to offset each

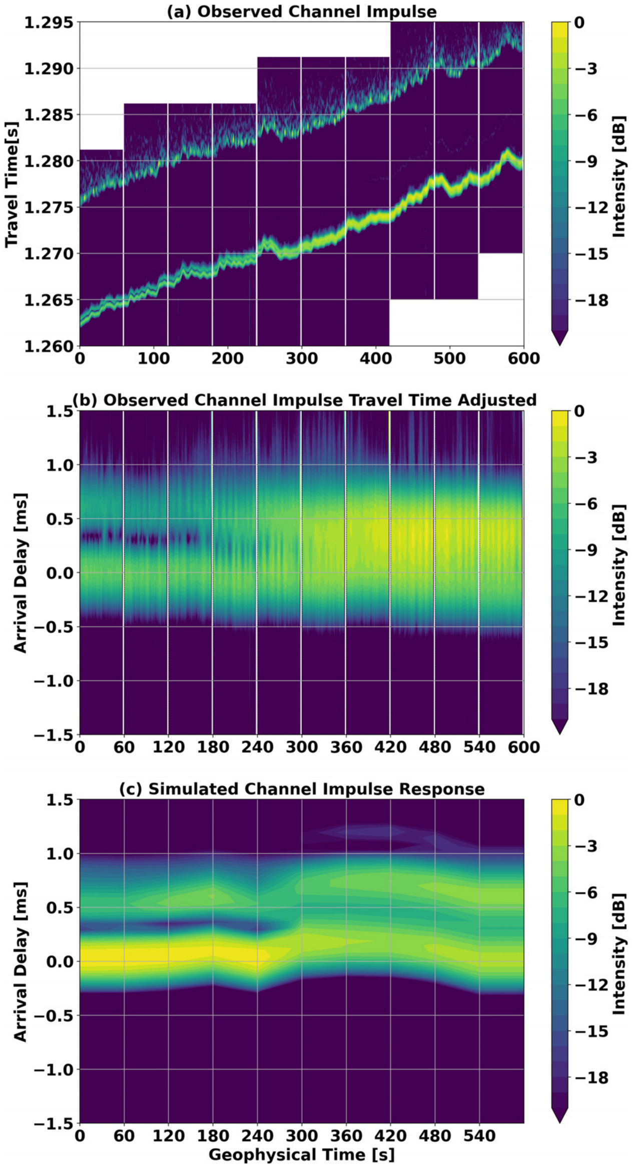

FIG. 14. (Color online) A time series of recorded (a), (b) and simulated (c) acoustic arrivals on a hydrophone at 129 m depth, including T2, on 17 May from 19:10 to 19:20 with intensity relative to the maximum arrival intensity shown in color and travel time in seconds on the vertical axis. (a) and (b) have a white gap every minute because the phase-coded arrivals are processed on minute intervals and the coded sequence length of 63.5 ms does not divide evenly into a minute. The travel time variability seen in (a) was removed in (b) by shifting each arrival by a time delay that maximizes the cross correlation with the previous arrival. The arrival time axis is shrunk in (b) to exclude the surface arrival. (c) A simulation of the refracted arrivals during the same time period using the series of sound-speed profiles measured at the same time as the transmissions shown in Fig. 5 (red profiles).

reception so that the first refracted arrival is centered at time-delay 0 in Fig. 14(b). The range was held constant in the simulation and so Fig. 14(c) is not travel time corrected with a cross correlation. There are slight changes in the travel time of the arrivals shown in Fig. 14(c) due to the changing sound-speed profile, but these are small compared to the change in travel time caused by the increasing range in the observed data.

The two observed arrivals in Fig. 14(b) with intensities of −20 dB or greater are separated by 0.6 ms at the beginning of the record. These two arrivals combine near minute five into a merged arrival with a broader peak. The merging of the two arrivals happened in under one minute and changed the intensity of the acoustic reception. The time evolution of the arrival intensity at 129 m depth was simulated, see Fig. 14(c), using a series of interpolated sound-speed profiles on 17 May from 19:10–19:20 sampled at one-minute intervals, which are highlighted with red in Fig. 5. The observed and simulated arrivals both display two separate arrivals that merge into a single arrival between minutes 4 and 5. Both the observed and simulated timefront over the full vertical span of the array preserve their "X-like" pattern, see Figs. 11(c) and 11(d), however, both timefronts moved upwards in arrival depth over the ten-minute interval. The movement of the timefront caused the overlapping arrivals seen in Figs. 7(c) and 7(d) at 130 m depth to move to a depth of 129 m where the series of arrivals are recorded in Figs. 14(b) and 14(c).

During this period of time, fine structure centered at 120 m was displaced upwards by 1 m highlighted by the green line in Fig. 5. Ray paths associated with the observed arrivals turn over at depths near 120 m, and so would be sensitive to a change in the position of the fine structure. Although, the range of the transmission is changing, Table I suggests that the arrival structure is more sensitive to perturbations in sound speed than range. The merging of two paths in Fig. 14(c) can be explained as an upwards shift of the timefront due to a meter scale displacement of the fine structure embedded in the sound-speed profile causing the interference point of the two arrivals in that timefront to sweep past the hydrophone at 129 m.

VI. DISCUSSION

The measurements in this paper identify sound-speed features that are important for modeling micro-multipathing. The rapidly repeated broad-band pulses are critical for resolving the path separation of the acoustic arrivals. The three examples of micro-multipathing in transmissions T1, T2, and T3 show receptions that have no interference, single interference, and multiple interferences, respectively. It was also typical to have multiple-interference arrivals for receptions with ranges greater than 2 km and less than 5 km, which are not shown in the paper. The short range of the transmissions is crucial for reducing the impact of range-dependent sound-speed perturbations in the channel. We would expect that at longer ranges, with multiple upper turning points, the paths would go through multiple triplications leading to saturation of the scintillation coefficient. This would increase the difficulty in sampling the sound speed and matching observed and modeled acoustic arrivals.

Full-wave simulations of mid-frequency acoustic propagation show triplication patterns similar to that of the ray simulation, which argues for the validity of arrivals that have distinct ray paths emanating from the triplication.

The full-wave simulations also show energy extending into the geometric shadow zone of the ray simulation which indicates that finite-wavelength effects are also relevant to micro-multipathing at mid-frequencies. We expect that at lower frequencies the agreement between full-wave and ray simulations would decrease as the Fresnel zone widens and diffraction smooths out the effects of small-scale features.

In general, reducing the relative curvature by smoothing the sound-speed profile reduces the number of caustics which increases the mismatch between the smoothed-profile simulations and the observations. There is not, however, a threshold for how much relative curvature is needed to form a caustic. The lack of a threshold is partially due to the dependence of caustic formation on the geometry of the ray paths between the source and receiver. For example, the triplicated arrivals in the simulated transmissions of T1 and T2 vanish when the depth-mean U_{10} is reduced to roughly 3.0 with a smoothing window of 12 m, see Fig. 10. In contrast, the simulated transmission of T3 which uses a smoothed sound-speed profile with similar depth-average U_{10} as T1 and T2 still contains triplicated arrivals. The slightly greater range of this transmission may be the reason for this difference, as triplications tend to grow with range. These observations only represent a small case study, not a comprehensive theory.

The importance of modeling additional ray paths related to strong second derivatives in sound speed lies in the interference of the arrivals. The interference of micro-multipath arrivals not only increases the scintillation but also creates ambiguity in the phase of the received acoustic pulse, see Figs. 13(c) and 13(e). As a consequence, caustics and micro-multipath interference from triplicated arrivals increase the sensitivity of the channel impulse response between source and receiver to the vertical position of those second derivatives. Weak vertical displacements of those second derivatives can cause strong fluctuations in acoustic intensity and phase, see Fig. 14, so internal waves with higher frequencies which tend to have lower energy can produce significant acoustic variability.

Further work is required to understand the correlation and time variability of micro-multipath arrivals specifically at short ranges where mid-frequency acoustic propagation is partially saturated—a regime of strong acoustic intensity variation due to strong focusing and interference.[13] Acoustic propagation modeling that includes realistic meter-scale vertical sound-speed variability could quantify statistics of micro-multipath interference. These statistics are important for understanding the scintillation as well as the phase decorrelation of the underwater acoustic channel.

ACKNOWLEDGMENTS

This research was supported by the Office of Naval Research under Grant No. N00014-19-1-2635. A special thanks to Matthew Dzieciuch who provided acoustic propagation modeling code for both RAM and ZRAY and to David Ensberg who processed the recorded MLS data from the experiment.

APPENDIX: COMPARISON METRICS

To quantify the difference between the observed and simulated arrivals over the array of hydrophones, the two-dimensional array data are converted into a single vector by concatenating the pressure record from each hydrophone along the time delay axis. The number of elements in the vector

$$N = m \cdot T \cdot f_t \tag{A1}$$

is equal to the time interval, T, times the sampling frequency, f_t, the number of hydrophone elements, m. Each pressure record is selected over a fixed $T = 5$ ms interval centered around the refracted arrivals. Those vectors of observed and simulated pressure were compared using the following metrics.

The Pearson correlation coefficient,

$$r = \frac{\sum_{i=1}^{N} (d_i - \bar{d})(\hat{d}_i - \bar{\hat{d}})}{\sqrt{\sum_{i=1}^{N} (d_i - \bar{d})^2 (\hat{d}_i - \bar{\hat{d}})^2}}, \tag{A2}$$

and the MSE,

$$MSE = \frac{1}{N} \sum_{i=1}^{N} (d_i - \hat{d}_i)^2, \tag{A3}$$

are calculated for $d_i = |p_i| / \boldsymbol{\Sigma}_{i=1}^{n} |p_i|$ the magnitude of the observed pressure p_i normalized by the sum over the entire array vector, and $\hat{d}_i = |\hat{p}_i| / \boldsymbol{\Sigma}_{i=1}^{n} |\hat{p}_i|$ the magnitude of the simulated pressure $\hat{p}_i$ normalized by the sum over the entire array vector. The MSE is reported scaled by the average squared amplitude inside the pulse arrival, d_i, as the Skill Score,

$$SS = 1 - \frac{MSE}{\frac{1}{N} \sum_{i=1}^{N} (d_i)^2}, \tag{A4}$$

and scaled by the average observed squared amplitude outside the pulse arrival, d_j,

$$MSE_r = 10 \log_{10} \left[\frac{MSE}{\frac{1}{M} \sum_{j=1}^{M} (d_j)^2} \right], \tag{A5}$$

which is the MSE relative to the observational noise. The observational noise is calculated by taking the average of the squared amplitude of the matched filter output before and after the pulse arrival. The ratio of the MSE to the noise is then reported in decibels.

[1] J. A. Colosi, *Sound Propagation through the Stochastic Ocean* (Cambridge University Press, New York, 2016), Chap. 1, pp. 14–20.

[2] G. Gopalakrishnan, B. D. Cornuelle, M. R. Mazloff, P. F. Worcester, and M. A. Dzieciuch, "State estimates and forecasts of the northern Philippine Sea circulation including ocean acoustic travel times," J. Atmos. Oceanic Technol. **38**(11), 1913–1933 (2021).

[3] F. S. Henyey, K. L. Williams, J. Yang, and D. Tang, "Simultaneous nearby measurements of acoustic propagation and high-resolution sound-speed structure containing internal waves," IEEE J. Oceanic Eng. **35**(4), 684–693 (2010).

[4] T. E. Ewart, J. E. Ehrenberg, and S. A. Reynolds, "Observations of the phase and amplitude of individual fermat paths in a multipath environment," J. Acoust. Soc. Am. **63**(6), 1801–1808 (1978).

[5] S. A. Reynolds, S. M. Flatté, R. Dashen, B. Buehler, and P. Maciejewski, "AFAR measurements of acoustic mutual coherence functions of time and frequency," J. Acoust. Soc. Am. **77**(5), 1723–1731 (1985).

[6] T. R. Osborn and C. S. Cox, "Oceanic fine structure," Geophys. Fluid Dyn. **3**(4), 321–345 (1972).

[7] B. Warren, *Evolution of Physical Oceanography* (MIT Press, Cambridge, 1981), Chap. 9, pp. 266–267.

[8] T. F. Duda, S. M. Flatté, J. A. Colosi, B. D. Cornuelle, J. A. Hildebrand, W. S. Hodgkiss, P. F. Worcester, B. M. Howe, J. A. Mercer, and R. C. Spindel, "Measured wave-front fluctuations in 1000-km pulse propagation in the Pacific Ocean," J. Acoust. Soc. Am. **92**(2), 939–955 (1992).

[9] T. E. Ewart, "A numerical simulation of the effects of oceanic finestructure on acoustic transmission," J. Acoust. Soc. Am. **67**(2), 496–503 (1980).

[10] T. F. Duda and J. B. Bowlin, "Ray-acoustic caustic formation and timing effects from ocean sound-speed relative curvature," J. Acoust. Soc. Am. **96**(2), 1033–1046 (1994).

[11] T. E. Ewart and S. A. Reynolds, "The mid-ocean acoustic transmission experiment, MATE," J. Acoust. Soc. Am. **75**(3), 785–802 (1984).

[12] P. F. Worcester, "Reciprocal acoustic transmission in a midocean environment," J. Acoust. Soc. Am. **62**(4), 895–905 (1977).

[13] J. A. Colosi, *Sound Propagation through the Stochastic Ocean* (Cambridge University Press, New York, 2016), Chap. 4, pp. 144–156.

[14] G. B. Deane, J. C. Preisig, C. T. Tindle, A. Lavery, and M. D. Stokes, "Deterministic forward scatter from surface gravity waves," J. Acoust. Soc. Am. **132**(6), 3673–3686 (2012).

[15] J. C. Preisig and G. B. Deane, "Surface wave focusing and acoustic communications in the surf zone," J. Acoust. Soc. Am. **116**(4), 2067–2080 (2004).

[16] W. H. Munk and P. F. Worcester, "Ocean acoustic tomography," Oceanography **1**(1), 8–10 (1988).

[17] K. L. Gemba, H. J. Vazquez, J. Fialkowski, G. F. Edelmann, M. A. Dzieciuch, and W. S. Hodgkiss, "A performance comparison between m-sequences and linear frequency-modulated sweeps for the estimation of travel-time with a moving source," J. Acoust. Soc. Am. **150**(4), 2613–2623 (2021).

[18] R. Pinkel, M. A. Goldin, J. A. Smith, O. M. Sun, A. A. Aja, M. N. Bui, and T. Hughen, "The Wirewalker: A vertically profiling instrument carrier powered by ocean waves," J. Atmos. Oceanic Technol. 28 **28**(3), 426–435 (2011).

[19] B. Zheng, A. J. Lucas, R. Pinkel, and A. Le Boyer, "Fine-scale velocity measurement on the Wirewalker wave-powered profiler," J. Atmos. Oceanic Technol. **39**(2), 133–147 (2022).

[20] A. Lucas, R. Pinkel, and M. Alford, "Ocean wave energy for long endurance, broad bandwidth ocean monitoring," Oceanography **30**(2), 126–127 (2017).

[21] J. M. Klymak, R. Pinkel, and L. Rainville, "Direct breaking of the internal tide near topography: Kaena Ridge, Hawaii," J. Phys. Oceanography **38**(2), 380–399 (2008).

[22] F. J. Millero, C.-T. Chen, A. Bradshaw, and K. Schleicher, "A new high pressure equation of state for seawater," Deep Sea Res. Part A. Oceanographic Res. Papers **27**(3), 255–264 (1980).

[23] L. Grare, N. M. Statom, N. Pizzo, and L. Lenain, "Instrumented wave gliders for air-sea interaction and upper ocean research," Front. Mar. Sci. **8**, 664728 (2021).

[24] L. Lenain and W. K. Melville, "Autonomous surface vehicle measurements of the ocean's response to tropical cyclone freda," J. Atmos. Oceanic Technol. **31**(10), 2169–2190 (2014).

[25] P. Dierckx, *Curve and Surface Fitting with Splines* (Oxford University Press, Oxford, 1995), Chap. 4, pp. 53–69.

[26] A. E. Gill, *Atmosphere-Ocean Dynamics* (Academic, New York, 1982), Vol. 30, Chap. 8, pp. 256–266.

[27] M. Dzieciuch, W. Munk, and D. L. Rudnick, "Propagation of sound through a spicy ocean, the SOFAR overture," J. Acoust. Soc. Am. **116**(3), 1447–1462 (2004).

[28] R. E. Todd, D. L. Rudnick, M. R. Mazloff, B. D. Cornuelle, and R. E. Davis, "Thermohaline structure in the California Current System: Observations and modeling of spice variance," J. Geophys. Res.: Oceans **117**(C2), C02008, https://doi.org/10.1029/2011JC007589 (2012).

[29] Y. A. Kravtsov and Y. I. Orlov, *Caustics, Catastrophes and Wave Fields* (Springer, Berlin, 1993), Chap. 2, pp. 17–26.

[30] J. A. Colosi, *Sound Propagation through the Stochastic Ocean* (Cambridge University Press, New York, 2016), Chap. 2, pp. 63–75.

[31] S. M. Flatte, R. D. Dashen, W. H. Munk, and F. Zachariasen, *Sound Transmission through a Fluctuating Ocean* (Stanford Research Institute, 1997), Chap. 7, 101–106.